IJMMM International Journal of Minerals, Metallurgy and Materials 矿物冶金与材料学报（英文版）

Tunable fabrication of single-crystalline $CsPbI_3$ nanobelts and their application as photodetectors

Tao Yang, Ya-peng Zheng, Kuo-Chih Chou, and Xin-mei Hou

Cite this article as:
Tao Yang, Ya-peng Zheng, Kuo-Chih Chou, and Xin-mei Hou, Tunable fabrication of single-crystalline $CsPbI_3$ nanobelts and their application as photodetectors, *Int. J. Miner. Metall. Mater.*, 28(2021), No. 6, pp. 1030-1037. https://doi.org/10.1007/s12613-020-2173-2

International Journal of Minerals, Metallurgy and Materials
Volume 28, Number 6, June 2021, Page 1030
https://doi.org/10.1007/s12613-020-2173-2

Tunable fabrication of single-crystalline $CsPbI_3$ nanobelts and their application as photodetectors

Tao Yang, Ya-peng Zheng, Kuo-Chih Chou, and Xin-mei Hou

Collaborative Innovation Center of Steel Technology, University of Science and Technology Beijing, Beijing 100083, China
(Received: 20 June 2020; revised: 20 August 2020; accepted: 25 August 2020)

Abstract: Lead halide perovskites have received increasing attention recently as a candidate material in various optoelectronic areas because of their high performance as light absorbers. Herein, we report the growth of $CsPbI_3$ nanobelts via a solution process. A single-crystalline $CsPbI_3$ nanobelt with uniform morphology can be achieved by controlling the amount of PbI_2. A single-crystalline $CsPbI_3$ nanobelt possesses a mean width, length, and thickness of 100 nm, 5 μm, and 20 nm, respectively. In this work, photodetectors (PDs) based on individual $CsPbI_3$ nanobelts are constructed and found to perform well with an external quantum efficiency and responsivity of 2.39×10^5% and 770 A/W, respectively. The PDs also show a high detectivity of up to 3.12×10^{12} Jones, which is at par with that of Si PDs. The PDs developed in this work exhibit great promise in various optoelectronic nanodevices.

Keywords: photodetector; cesium lead triiodide; perovskite; nanobelt; detectivity

1. Introduction

Lead halide perovskites have received increasing attention recently because of their high performance as light absorbers. For example, their photoconversion efficiency can reach 22.1%, which suggests their great potential to be applied to the optoelectronic field [1–2]. However, hybrid perovskites have poor long-term stability due to the decomposition and volatilization of the organic components within them [3–4]. All-inorganic perovskites are more stable than organic–inorganic hybrid perovskites, and they exhibit broad chemical/physical tunability and excellent charge transport. Therefore, all-inorganic perovskites have been widely applied in the optoelectronic field in various forms, such as lasers [5], photodetectors (PDs) [6–7], light-emitting diodes [8], and photovoltaic solar cells [9–10], PDs are particularly regarded as a hot topic because of their wide applications. For instance, Li *et al.* [11] reported $CsPbBr_3$ microparticles with a detectivity of 6.1×10^{10} Jones. Saidaminov *et al.* [12] reported $CsPbBr_3$ bulk single crystals with a detectivity of 1.7×10^{11} Jones. Waleed *et al.* [13] reported $CsPbI_3$ nanoarray PDs with a high detectivity of up to 1.57×10^{12} Jones. However, three-dimensional perovskite bulks and polycrystalline films possess low photoconversion efficiencies because of the undesired charge recombination at grain boundaries and the low carrier mobility (<10 $cm^2 \cdot V^{-1} \cdot s^{-1}$) [14–15]. Improving perovskite PDs remains a great challenge today.

Compared with three-dimensional perovskite bulks and polycrystalline films, one-dimensional single-crystalline perovskite nanobelts with well structures possess longer carrier diffusion lengths, larger carrier mobility, and higher photoluminescence quantum yields [16–18]. Moreover, one-dimensional perovskite nanobelts can provide relatively direct charge transport pathways, which can benefit the collection of carriers. In this work, we report the exploration of PDs based on a single $CsPbI_3$ nanobelt. First, the high-purity single-crystalline $CsPbI_3$ nanobelts were synthesized via a solution process using different amounts of PbI_2. Second, individual $CsPbI_3$ nanobelt PDs were constructed via photolithography, magnetron sputtering, and lift-off process. Third, response repeatability, switching ratio, response time, external quantum efficiency, spectral responsivity, and detectivity of PDs were measured. At last, the mechanism of the outstanding performance of the nanobelt PDs was discussed.

2. Experimental

2.1. Materials

All chemicals were used without any further purification. Hexane (anhydrous, 95%), oleylamine (OlAm, 70%), 1-octadecene (ODE, 90%), toluene (anhydrous, 95%), hexanoic acid (≥99%), octanoic acid (99%), octylamine (OctAm,

Corresponding author: Xin-mei Hou E-mail: houxinmeiustb@ustb.edu.cn

99%), and oleic acid (OA, 90%) were purchased from Sinopharm Chemical Reagent Beijing Co., Ltd., China. Cesium carbonate (Cs_2CO_3, 99%) and lead(II) iodide (PbI_2, 99%) were purchased from Aladdin Reagent Co., Ltd., China.

2.2. Preparation of cesium-oleate solution

Briefly, 1.2 mL of OA, 0.4 g of Cs_2CO_3, and 15 mL of ODE were added into a three-neck flask, degassed, and dried under vacuum at 120°C for 60 min. The mixture was then heated under N_2 to 150°C until all Cs_2CO_3 dissolved into OA.

2.3. Synthesis of $CsPbI_3$ nanobelt

Exactly 8 mL of ODE, 0.069 g of PbI_2, and proper amounts of OlAm and OctAm were added into a 25 mL three-neck flask. The mixture was dried at 100°C for 45 min under vacuum to form a cloudy solution. Thereafter, the mixture was heated under N_2 to 120°C and held for 10 min. Exactly 0.6 mL of Cs-oleate solution was injected in a three-neck flask. The nanobelt was then allowed to grow for 50 min at 120°C. Immediately following the synthesis, the reaction was quenched by an ice water bath and centrifuged at 10000 r/min for 5 min. The nanobelt was isolated through centrifugation at 7000 r/min for 3 min. The obtained nanobelt was redispersed in hexane/toluene for later use. All procedures were conducted under ambient conditions.

2.4. Photodetector (PD) device fabrication and measurements

Individual $CsPbI_3$ nanobelt PDs were fabricated. Through photolithography, magnetron sputtering, and lift-off process, interdigitated Au electrodes (100 nm) with 4 μm separation were patterned on top of a Si substrate with a 300 nm SiO_2 layer. Then, the $CsPbI_3$ nanobelt in hexane was deposited dropwise on the electrodes.

2.5. Photoelectric property measurement and structural characterization

All experiments were conducted under ambient conditions at room temperature. X-ray diffraction (XRD, D8 Advance, Bruker, Germany) with Cu K_α radiation (λ = 0.15406 nm), transmission electron microscopy (TEM, JEM-2010, JEOL, Japan), and field-emission scanning electron microscopy (S-4800, Hitachi, Japan) together with energy-dispersive X-ray spectroscopy were used to characterize the nanobelt. A UV–vis scanning spectrophotometer (U-3900, HITACHI, Japan) was used to obtain the UV–vis spectrum of the nanobelt. A four-probe station with a semiconductor characterization system (Keithley 4200-CSC) was used to obtain the electrical and optoelectronic data of the PDs. A 500 W Xenon arc lamp coupled to an Acton Research monochromator with order-sorting filters was used as the light source. Light intensity was measured with an OAI-306 power meter. The laser had a wavelength of 405 nm, maximum power of 200 mW, and a spot size measuring 4 mm in diameter.

3. Results and discussion

3.1. Tunable fabrication and characterization

In our recent work, we reported that the amount of PbI_2 plays a fundamental role in the preparation of defect-free and high-quality one-dimensional $CsPbI_3$ nanobelts [7]. Herein, the microstructure of the as-prepared $CsPbI_3$ was revealed by the scanning electron microscope (SEM) techniques. When 96 mg of PbI_2 was introduced (Figs. 1(a) and 1(b)), nanorods

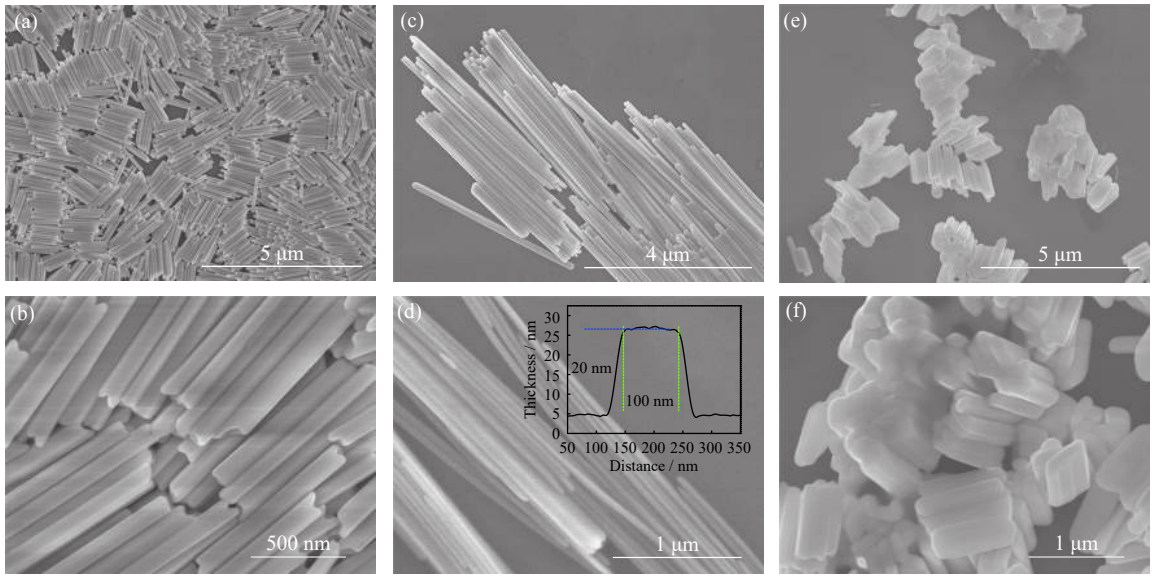

Fig. 1. SEM images of the obtained $CsPbI_3$ nanocrystal with varying amounts of introduced PbI_2: (a, b) 96 mg; (c, d) 87 mg; (e, f) 105 mg. Inset of (d) is the typical thickness and width measurement result of nanobelts from an atomic force microscope.

with a uniform diameter of 150 nm and an average length of 2 μm were obtained. When 87 mg of PbI_2 was introduced (Figs. 1(c) and 1(d)), the resultant products were pure nanobelts with a mean width, length, and thickness of 100 nm, 5 μm, and 20 nm, respectively. The typical thickness and width measured by an atomic force microscope were approximately 20 nm and 100 nm, respectively (inset of Fig. 1(d)). The thickness/width (t/w) ratio was above 0.2. However, when the amount of introduced PbI_2 was increased to 105 mg (Figs. 1(e) and 1(f)), the as-synthesized nanorods began to aggregate and conglutinate.

As shown in Fig. 2, strong diffraction peaks ascribed to the orthorhombic phase of $CsPbI_3$ (JCPDS Card No. 18-0376) were observed in the XRD patterns of the obtained samples. Generally, $CsPbI_3$ undergoes a one-phase transition under a reduced temperature [19], that is, its color changes from dark to yellow, and it exhibits a cubic-orthorhombic structure (328°C) [20]. As shown in Fig. 2, the $CsPbI_3$ nanobelt was confirmed to be in the orthorhombic phase on the basis of the XRD pattern of the crystal and the yellow color.

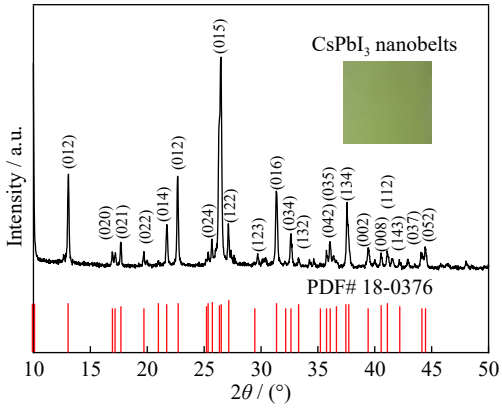

Fig. 2. XRD pattern of nanobelt. The inset is a photograph of the $CsPbI_3$ nanobelt dispersed in hexane.

The single-crystalline nature and chemical composition of the nanobelt were confirmed using TEM and energy dispersive X-Ray (EDX). As shown in Figs. 3(a)–3(c), the morphology of the nanobelt indicated a typical width of 100 nm. A d spacing of ~0.479 nm, which corresponded to (100) planes, was observed in the high resolution transmission electron microscope (HRTEM) result (Fig. 3(d)). The selected area electron diffraction (SAED) pattern (Fig. 3(e)) can be indexed to an orthorhombic structure, which indicated its single-crystalline nature. The EDX pattern of the single nanobelt revealed Cs, Pb, and I elements with a quantified molar ratio of 1:1:3, which further confirmed that the nanobelt was $CsPbI_3$. The single-crystalline nature and suitable one-dimensional morphology of the nanobelt provide PDs with capabilities for high-quality charge carrier transmission and complete light absorption.

The optoelectronic properties of the $CsPbI_3$ nanobelt were investigated on the basis of the UV–vis absorption spectrum. As shown in Fig. 4(a), the absorbance peak of the $CsPbI_3$ nanobelt was located at 405 nm. Fig. 4(b) shows the $(\alpha hv)^2$ versus E_g plot (α is absorption coefficient, h is Planck's constant, v is frequency of light, E_g is band gap) for the $CsPbI_3$ nanobelt. A direct bandgap of about 2.60 eV was observed. The $CsPbI_3$ nanobelt can thus be used as a violet PD due to the location of the absorbance at 405 nm.

3.2. Photodetector characterization

Utilizing the as-grown $CsPbI_3$ nanobelt, we fabricated PDs with a low-dimensional structure. Figs. 4(c) and 4(d) present

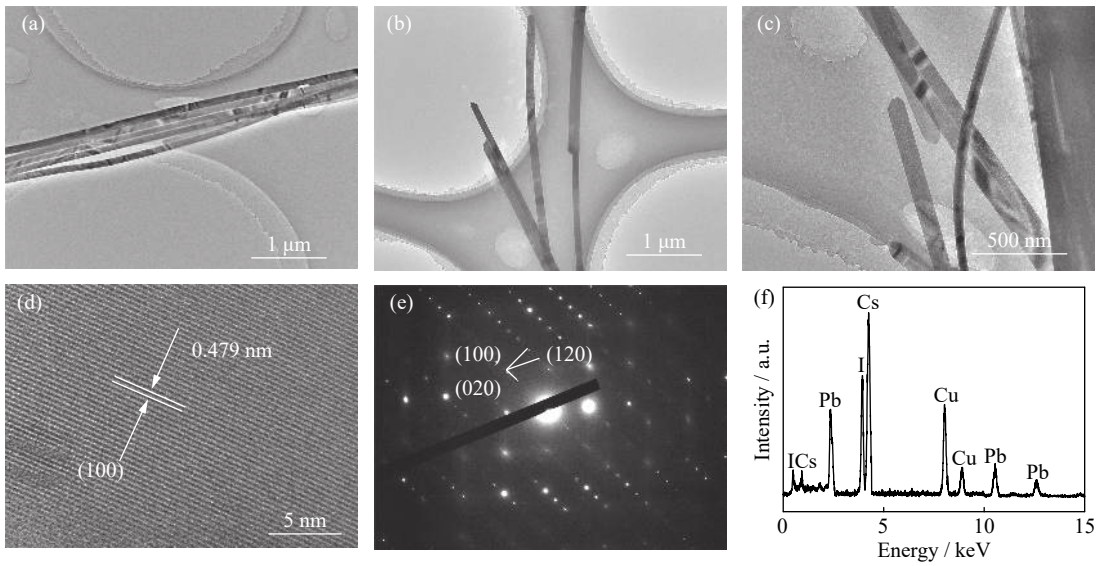

Fig. 3. (a–c) TEM images of $CsPbI_3$ nanobelt; (d) a representative HRTEM image of $CsPbI_3$ nanobelt; (e) SAED pattern of $CsPbI_3$ nanobelt; (f) typical EDX spectrum of the nanobelt.

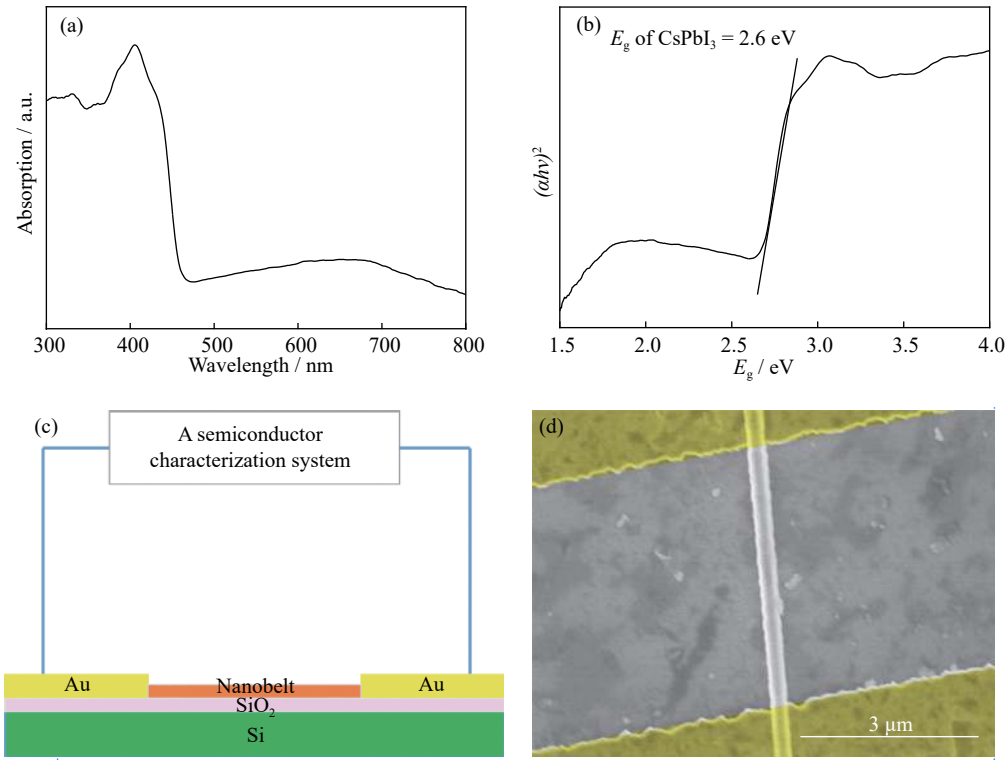

Fig. 4. (a) UV–vis spectrum of $CsPbI_3$ nanobelt; (b) $(\alpha hv)^2$ vs. E_g plot; (c) schematic of single $CsPbI_3$ nanobelt PD; (d) SEM image of individual nanobelt PD.

the schematic of the individual $CsPbI_3$ nanobelt PD and its SEM image. Fig. 5(a) shows the comparative current–voltage (*I–V*) characteristics of the $CsPbI_3$ nanobelt PD under dark conditions and a light of 405 nm with an average power of 10 mW/cm^2. The dark current of the PD was lower than 0.19 nA at 2.0 V. When the device was illuminated under a light above the bandgap E_g of 3.06 eV, the photocurrent magnitude of the $CsPbI_3$ nanobelt PD was two orders higher than that of the dark current. The photocurrent approached 7.90 nA at a bias of 2.0 V. The asymmetric and nonlinear *I–V* curves (Fig. 5(b)) indicated that Schottky contact occurred between the electrodes and the $CsPbI_3$ nanobelt.

Response repeatability is a key parameter for PDs. The time–response of the $CsPbI_3$ nanobelt PD was measured by periodically turning on and off the 405 nm light at a voltage of 2.0 V. As shown in Fig. 4(c), when the light irradiation was on and off, the current exhibited two distinct states, namely, dark current of 0.19 nA and increased photocurrent of 7.90 nA, respectively. In switching the light on/off for more than 200 cycles, the $CsPbI_3$ nanobelt PDs exhibited excellent stability and reproducibility. The switching ratio (δ_{SR}) was calculated as:

$$\delta_{SR} = \frac{I_{ph}}{I_{dark}} = \frac{I_{on} - I_{off}}{I_{off}} \tag{1}$$

where I_{dark} is the dark current, I_{off} is the current of turning off the light, I_{ph} is the photocurrent under 405 nm light (10 mW/cm^2) and I_{on} is the current of turning on the light. The δ_{SR} of the nanobelt PD reached 41. The huge gap in δ_{SR} was related to light absorptivity, which is influenced by the types of materials.

Response time is another key parameter for PDs. Herein, the response time was measured by using 405 nm continuous laser triggers with a pulse width of 0.05 Hz. The sharp current from one state to another indicated an extremely fast response time. The recovery time (τ_{off}) and response time (τ_{on}) were defined as the time for the maximum photocurrent to reach 10% of the dark current or vice versa (90%). As shown in Fig. 5(d), the recovery time and response time of the nanobelt PD were measured as ~0.5 s and 0.5 s, respectively. The single-crystalline nature and one-dimensional morphology of the nanobelt that favor carrier transport led to the fast response time.

External quantum efficiency (η_{EQE}) and spectral responsivity (R_λ) are two important parameters for PDs [21–22], and they are respectively calculated as

$$R_\lambda = \frac{\Delta I}{L_{light}} = \frac{I_{on} - I_{off}}{PA} \tag{2}$$

$$\eta_{EQE} = \frac{hc}{e\lambda} R_\lambda \tag{3}$$

where A is the effective area of the detector, P is the light power intensity, L_{light} is the incident light intensity, and ΔI is the difference between the photocurrent and the dark current.

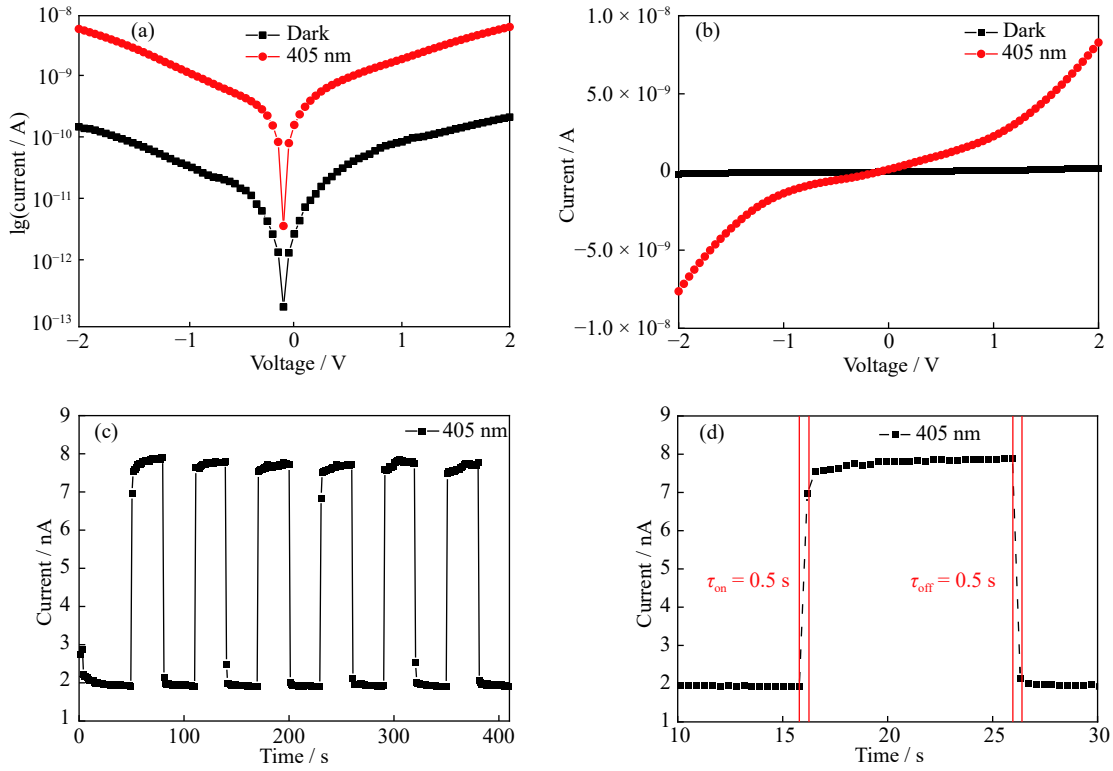

Fig. 5. (a) Logarithmic *I*–*V* under 405 nm light and dark conditions; (b) *I*–*V* characteristics under 405 nm light and dark conditions; (c) reproducible on/off switching under 405 nm light; (d) response time (recovery time (τ_{off}) and response time (τ_{on})) under 405 nm light pulse chopped at a 0.05 Hz frequency.

λ is the exciting wavelength, e is the electron charge, c is the velocity of light, and h is Planck's constant. Under 405 nm light with 10 mW/cm^2 under an applied voltage of 2.0 V, the calculated R_λ and η_{EQE} of the PD (Figs. 6(a) and 6(b)) were as high as 770.65 A/W and 2.39 × 10^5%, respectively.

The wavelength selectivity of a PD determines the applied wavelength range of the device. Fig. 6(a) shows the spectral response of the nanobelt PD to the wavelength changing from 250 to 600 nm at a bias of 2.0 V. The ratio between R_λ (405 nm, 770.65 A/W) and R_λ (500 nm, 0.46 A/W) was approximately 1675.32, which indicated the high spectral selectivity and sensitivity of the PD. Hence, as shown in Fig. 6(b), the nanobelt PD developed herein can be used as a typical ultraviolet (UV) and blue light PD.

Detectivity (D^*) is given by

$$D^* = \frac{(Af)^{\frac{1}{2}}}{\frac{R_\lambda}{I_n}} \tag{4}$$

where I_n is the noise current and f is the electrical bandwidth. D^* can be expressed as follows when the shot noise dominates the dark current:

$$D^* = \frac{R_\lambda}{\left(2e\frac{I_{off}}{A}\right)^{\frac{1}{2}}} \tag{5}$$

Evidently, the smaller the dark current is, the better the detection of weak optical signals will be. Avoiding any leakage current during operation is extremely important to obtain a small I_{off}. The effective ways to obtain a small I_{off} include maintaining good single-crystalline quality, low thermal emission (recombination) rates, and low trap density of semiconductors. For the nanobelt PD in this work, the specific detectivity was calculated to be 3.12 × 10^{12} Jones (Jones = cm·Hz$^{1/2}$·W^{-1}) at 405 nm. The detectivity of the nanobelt PD approached 10^{12} Jones from 250 to 450 nm at 2.0 V and is thus at par with the detectivity of Si PDs [23–24].

In addition to the wavelength of light, light power intensity is another key influencing factor for the photocurrent of PDs. The time–response curves of the nanobelt PD are plotted with light power intensity in Fig. 6(c). As the 405 nm light power intensity increased from 3 to 16 mW/cm^2 at a voltage of 2.0 V, the photocurrent of the nanobelt PD increased from 3.84 to 9.33 nA. This result agreed with the fact that the absorbed photon flux was proportional to the photoinduced carrier efficiency. Even after being subjected to the largest photocurrent for a long period, the photocurrent of the PD remained stable and exhibited good repeatability. The dependence of the photocurrent on light power intensity can be expressed by a power law: $I_{ph} = BP^\theta$ [25], where θ is the exponent ($0.5 < \theta < 1$), B is a constant for a given wavelength; θ = 0.53 was obtained (Fig. 6(d)) by fitting the curve in Fig. 6(c). The non-unity exponent suggested a complex pro-

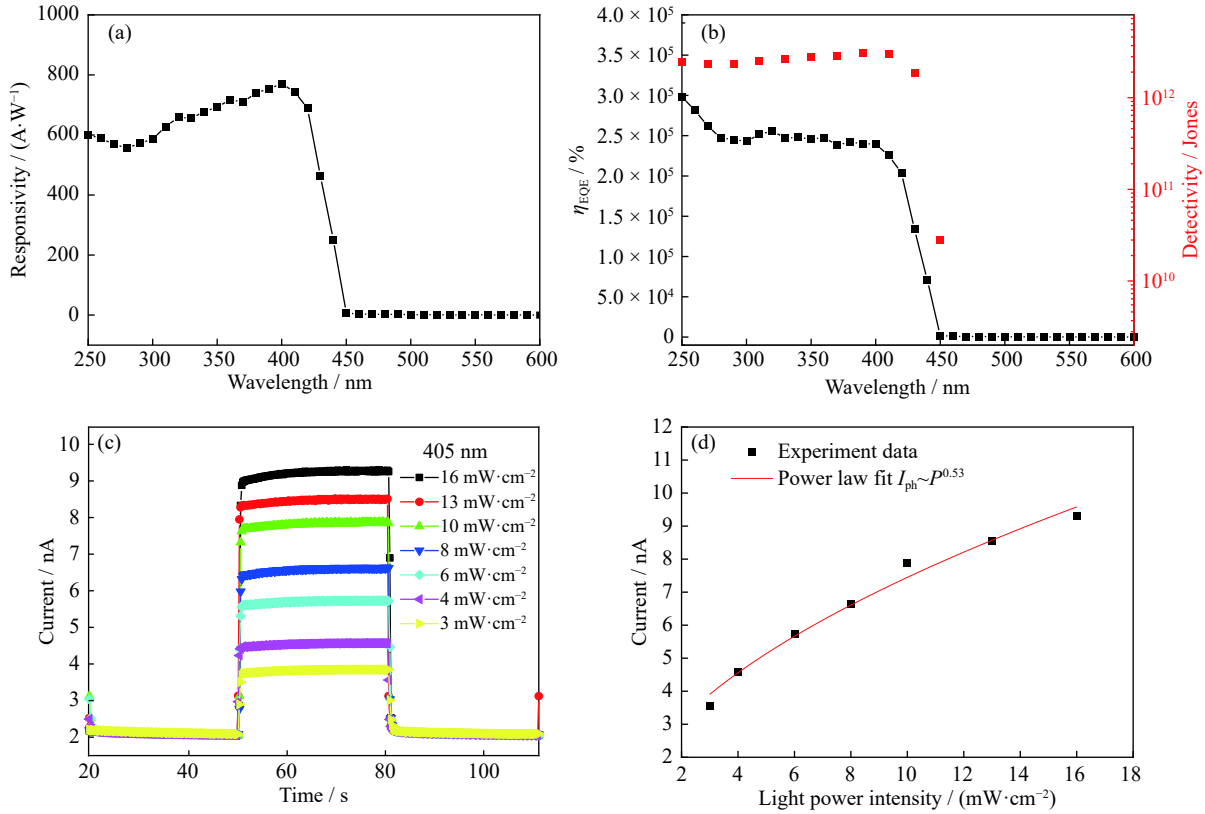

Fig. 6. (a) Spectral response of PD from 250 to 600 nm; (b) detectivity and η_{EQE} of PD at different wavelengths; (c) time–response curves of nanobelt PD under different light power intensities; (d) relationship between light power intensity and photocurrents.

cess, which included electron-hole generation and trapping and recombination within the $CsPbI_3$ nanobelt [26–28].

Under 405 nm light illumination at a bias of 2.0 V, R_λ, D^*, and η_{EQE} reached 770 A/W, 3.12×10^{12} Jones, and 2.39×10^5%, respectively. In the range of 300–450 nm, the detectivity of the PD exceeded 10^{12} Jones and is thus at par with the detectivity of Si PDs (i.e., 10^{12} Jones) [23–24]. As listed in Table 1, the detectivity is comparable to the best detectivities of pristine perovskite PDs ever reported.

The outstanding performance of the nanobelt PD is mainly attributed to the following reasons. First, the $CsPbI_3$ nanobelt has a low recombination of charge carriers, low density of defects, short paths for carrier transfer, and high absorption coefficient; these properties could result in a strong photoelectric effect. Second, the single-crystal $CsPbI_3$ nanobelt possesses high single crystallinity. Therefore, the recombination of charge carriers is limited due to the low density of defects of the single-crystalline structure [35]. Third, the absorption coefficient of the perovskite reaches the order of 10^4 cm^{-1} because of the direct bandgap nature of the electronic transition. Therefore, almost all light can be absorbed by the $CsPbI_3$ nanobelt [23].

Table 1. Typical perovskite PDs reported in the literature

Photodetector	Bias / V	Responsivity / (A·W^{-1})	Detectivity / Jones	Ref.
$CH_3NH_3PbI_3$ film	3	3.49	—	[29]
$CH_3NH_3PbI_3$ network	10	0.1	1.02×10^{12}	[30]
$CsPbBr_3$ microparticles	10	0.18	6.1×10^{10}	[11]
$CsPbBr_3$ nanoparticles/Au nanocrystals	2	0.01	1.68×10^9	[31]
$CsPbBr_3$ thin films	6	55	9×10^{12}	[32]
$CsPbI_3$ nanoarrays	1	0.0067	1.57×10^{12}	[13]
$CsPbBr_3$ nanosheets/carbon nanotubes	10	31.1	—	[33]
$CsPbBr_3$ nanoplatelets	1.5	34	7.5×10^{12}	[34]
$CsPbBr_3$ bulk single crystals	0	0.028	1.7×10^{11}	[12]
$CsPbI_3$ nanobelt	2	770.65	3.12×10^{12}	This work

4. Conclusion

In summary, we demonstrated the growth of an all-inorganic $CsPbI_3$ perovskite nanobelt via a solution process. And the amount of introduced PbI_2 played a fundamental role in morphological regulation of the obtained single-crystalline nanobelt. When 87 mg of PbI_2 was introduced, the resultant products were pure nanobelts with a mean width, length, and thickness of 100 nm, 5 μm, and 20 nm, respectively. The PDs based single $CsPbI_3$ nanobelt showed an outstanding performance with an external quantum efficiency of 2.39×10^5%, a responsivity of 770 A/W and a detectivity of 3.12×10^{12} Jones. They are at par with the detectivity of Si PDs. The excellent performance of the nanobelt PDs are mainly attributed the intrinsic properties of $CsPbI_3$, high crystallinity of $CsPbI_3$, and special morphology of nanobelt.The overall excellent performance of the $CsPbI_3$ nanobelt makes it an excellent candidate material for various optoelectronic areas.

Acknowledgements

This work was financially supported by the National Natural Science Foundation of China (Nos. 51974021 and 51902020), the Fundamental Research Funds for the Central Universities (Nos. FRF-TP-18-045A1 and FRF-TP-19-004B2Z), the National Postdoctoral Program for Innovative Talents (BX20180034), and the China Postdoctoral Science Foundation (Grant No. 2018M641192).

References

[1] N.J. Jeon, J.H. Noh, W.S. Yang, Y.C. Kim, S. Ryu, J. Seo, and S.I. Seok, Compositional engineering of perovskite materials for high-performance solar cells, *Nature*, 517(2015), No. 7535, p. 476.

[2] L. Protesescu, S. Yakunin, M.I. Bodnarchuk, F. Krieg, R. Caputo, C.H. Hendon, R.X. Yang, A. Walsh, and M.V. Kovalenko, Nanocrystals of cesium lead halide perovskites ($CsPbX_3$, X = Cl, Br, and I): Novel optoelectronic materials showing bright emission with wide color gamut, *Nano Lett.*, 15(2015), No. 6, p. 3692.

[3] B. Conings, J. Drijkoningen, N. Gauquelin, A. Babayigit, J. D'Haen, L. D'Olieslaeger, A. Ethirajan, J. Verbeeck, J. Manca, E. Mosconi, F. de Angelis, and H.G. Boyen, Intrinsic thermal instability of methylammonium lead trihalide perovskite, *Adv. Energy Mater.*, 5(2015), No. 15, art. No. 1500477.

[4] J. Yang, B.D. Siempelkamp, D. Liu, and T.L. Kelly, Investigation of $CH_3NH_3PbI_3$ degradation rates and mechanisms in controlled humidity environments using *in situ* techniques, *ACS Nano*, 9(2015), No. 2, p. 1955.

[5] P. Liu, X.X. He, J.H. Ren, Q. Liao, J.N. Yao, and H.B. Fu, Organic–inorganic hybrid perovskite nanowire laser arrays, *ACS Nano*, 11(2017), No. 6, p. 5766.

[6] M.I. Saidaminov, M.A. Haque, M. Savoie, A.L. Abdelhady, N. Cho, I. Dursun, U. Buttner, E. Alarousu, T. Wu, and O.M. Bakr, Perovskite photodetectors operating in both narrowband and broadband regimes, *Adv. Mater.*, 28(2016), No. 37, p. 8144.

[7] T. Yang, Y.P. Zheng, Z.T. Du, W.N. Liu, Z.B. Yang, F.M. Gao, L. Wang, K.C. Chou, X.M. Hou, and W.Y. Yang, Superior photodetectors based on all-inorganic perovskite $CsPbI_3$ nanorods with ultrafast response and high stability, *ACS Nano*, 12(2018), No. 2, p. 1611.

[8] L. Meng, E.P. Yao, Z.R. Hong, H.J. Chen, P.Y. Sun, Z.L. Yang, G. Li, and Y. Yang, Pure formamidinium-based perovskite light-emitting diodes with high efficiency and low driving voltage, *Adv. Mater.*, 29(2017), No. 4, art. No. 1603826.

[9] M. Saliba, T. Matsui, K. Domanski, J.Y. Seo, A. Ummadisingu, S.M. Zakeeruddin, J.P. Correa-Baena, W.R. Tress, A. Abate, A. Hagfeldt, and M. Gratzel, Incorporation of rubidium cations into perovskite solar cells improves photovoltaic performance, *Science*, 354(2016), No. 6309, p. 206.

[10] D.W. Zhao, Y. Yu, C.L. Wang, W.Q. Liao, N. Shrestha, C.R. Grice, A.J. Cimaroli, L. Guan, R.J. Ellingson, K. Zhu, X.Z. Zhao, R.G. Xiong, and Y.F. Yan, Low-bandgap mixed tin–lead iodide perovskite absorbers with long carrier lifetimes for all-perovskite tandem solar cells, *Nat. Energy*, 2(2017), No. 4, art. No. 17018.

[11] X.M. Li, D.J. Yu, F. Cao, Y. Gu, Y. Wei, Y. Wu, J.Z. Song, and H.B. Zeng, Healing all-inorganic perovskite films via recyclable dissolution–recyrstallization for compact and smooth carrier channels of optoelectronic devices with high stability, *Adv. Funct. Mater.*, 26(2016), No. 32, p. 5903.

[12] M.I. Saidaminov, M.A. Haque, J. Almutlaq, S. Sarmah, X.H. Miao, R. Begum, A.A. Zhumekenov, I. Dursun, N. Cho, B. Murali, O.F. Mohammed, T. Wu, and O.M. Bakr, Inorganic lead halide perovskite single crystals: Phase-selective low-temperature growth, carrier transport properties, and self-powered photodetection, *Adv. Opt. Mater.*, 5(2017), No. 2, art. No. 1600704.

[13] A. Waleed, M.M. Tavakoli, L.L. Gu, S. Hussain, D.Q. Zhang, S. Poddar, Z.Y. Wang, R.J. Zhang, and Z.Y. Fan, All inorganic cesium lead iodide perovskite nanowires with stabilized cubic phase at room temperature and nanowire array-based photodetectors, *Nano Lett.*, 17(2017), No. 8, p. 4951.

[14] W.Y. Nie, H. Tsai, R. Asadpour, J.C. Blancon, A.J. Neukirch, G. Gupta, J.J. Crochet, M. Chhowalla, S. Tretiak, M.A. Alam, H.L. Wang, and A.D. Mohite, Solar cells. High-efficiency solution-processed perovskite solar cells with millimeter-scale grains, *Science*, 347(2015), No. 6221, p. 522.

[15] Q.F. Dong, Y.J. Fang, Y.C. Shao, P. Mulligan, J. Qiu, L. Cao, and J.S. Huang, Solar cells. Electron-hole diffusion lengths > 175 μm in solution-grown $CH_3NH_3PbI_3$ single crystals, *Science*, 347(2015), No. 6225, p. 967.

[16] W. Deng, X.J. Zhang, L.M. Huang, X.Z. Xu, L. Wang, J.C. Wang, Q.X. Shang, S.T. Lee, and J.S. Jie, Aligned single-crystalline perovskite microwire arrays for high-performance flexible image sensors with long-term stability, *Adv. Mater.*, 28(2016), No. 11, p. 2201.

[17] J. Xing, X.F. Liu, Q. Zhang, S.T. Ha, Y.W. Yuan, C. Shen, T.C. Sum, and Q.H. Xiong, Vapor phase synthesis of organometal halide perovskite nanowires for tunable room-temperature nanolasers, *Nano Lett.*, 15(2015), No. 7, p. 4571.

[18] H.M. Zhu, Y.P. Fu, F. Meng, X.X. Wu, Z.Z. Gong, Q. Ding, M.V. Gustafsson, M.T. Trinh, S. Jin, and X.Y. Zhu, Lead halide perovskite nanowire lasers with low lasing thresholds and high quality factors, *Nat. Mater.*, 14(2015), No. 6, p. 636.

[19] D.M. Trots and S.V. Myagkota, High-temperature structural evolution of caesium and rubidium triiodoplumbates, *J. Phys. Chem. Solids*, 69(2008), No. 10, p. 2520.

[20] C.K. Møller, Crystal structure and photoconductivity of cæsium plumbohalides, *Nature*, 182(1958), No. 4647, p. 1436.
[21] P.A. Hu, Z.Z. Wen, L.F. Wang, P.H. Tan, and K. Xiao, Synthesis of few-layer GaSe nanosheets for high performance photodetectors, *ACS Nano*, 6(2012), No. 7, p. 5988.
[22] L. Ma, W. Hu, Q.L. Zhang, P.Y. Ren, X.J. Zhuang, H. Zhou, J.Y. Xu, H.L. Li, Z.P. Shan, X.X. Wang, L. Liao, H.Q. Xu, and A.L. Pan, Room-temperature near-infrared photodetectors based on single heterojunction nanowires, *Nano Lett.*, 14(2014), No. 2, p. 694.
[23] L.T. Dou, Y. Yang, J.B. You, Z.R. Hong, W.H. Chang, G. Li, and Y. Yang, Solution-processed hybrid perovskite photodetectors with high detectivity, *Nat. Commun.*, 5(2014), art. No. 5404.
[24] X. Gong, M.H. Tong, Y.J. Xia, W.Z. Cai, J.S. Moon, Y. Cao, G. Yu, C.L. Shieh, B. Nilsson, and A.J. Heeger, High-detectivity polymer photodetectors with spectral response from 300 nm to 1450 nm, *Science*, 325(2009), No. 5948, p. 1665.
[25] S. Panigrahi and D. Basak, Core-shell TiO_2@ZnO nanorods for efficient ultraviolet photodetection, *Nanoscale*, 3(2011), No. 5, p. 2336.
[26] H. Kind, H. Yan, B. Messer, M. Law, and P. Yang, Nanowire ultraviolet photodetectors and optical switches, *Adv. Mater.*, 14(2002), No. 2, p. 158.
[27] C. Soci, A. Zhang, B. Xiang, S.A. Dayeh, D.P.R. Aplin, J. Park, X.Y. Bao, Y.H. Lo, and D. Wang, ZnO nanowire UV photodetectors with high internal gain, *Nano Lett.*, 7(2007), No. 4, p. 1003.
[28] H. Liu, Z.M. Zhang, L.F. Hu, N. Gao, L.W. Sang, M.Y. Liao, R.Z. Ma, F.F. Xu, and X.S. Fang, New UV-A photodetector based on individual potassium niobate nanowires with high performance, *Adv. Opt. Mater.*, 2(2014), No. 8, p. 771.
[29] X. Hu, X.D. Zhang, L. Liang, J. Bao, S. Li, W.L. Yang, and Y. Xie, High-performance flexible broadband photodetector based on organolead halide perovskite, *Adv. Funct. Mater.*, 24(2014), No. 46, p. 7373.
[30] H. Deng, X.K. Yang, D.D. Dong, B. Li, D. Yang, S.J. Yuan, K.K. Qiao, Y.B. Cheng, J. Tang, and H.S. Song, Flexible and semitransparent organolead triiodide perovskite network photodetector arrays with high stability, *Nano Lett.*, 15(2015), No. 12, p. 7963.
[31] Y.H. Dong, Y. Gu, Y.S. Zou, J.Z. Song, L.M. Xu, J.H. Li, J. Xue, X.M. Li, and H.B. Zeng, Improving all-inorganic perovskite photodetectors by preferred orientation and plasmonic effect, *Small*, 12(2016), No. 40, p. 5622.
[32] Y. Li, Z.F. Shi, S. Li, L.Z. Lei, H.F. Ji, D. Wu, T.T. Xu, Y.T. Tian, and X.J. Li, High-performance perovskite photodetectors based on solution-processed all-inorganic $CsPbBr_3$ thin films, *J. Mater. Chem. C*, 5(2017), No. 33, p. 8355.
[33] X.M. Li, D.J. Yu, J. Chen, Y. Wang, F. Cao, Y. Wei, Y. Wu, L. Wang, Y. Zhu, Z.G. Sun, J.P. Ji, Y.L. Shen, H.D. Sun, and H.B. Zeng, Constructing fast carrier tracks into flexible perovskite photodetectors to greatly improve responsivity, *ACS Nano*, 11(2017), No. 2, p. 2015.
[34] X.H. Liu, D.J. Yu, F. Cao, X.M. Li, J.P. Ji, J. Chen, X.F. Song, and H.B. Zeng, Low-voltage photodetectors with high responsivity based on solution-processed micrometer-scale all-inorganic perovskite nanoplatelets, *Small*, 13(2017), No. 25, art. No. 1700364.
[35] M. Shoaib, X.H. Zhang, X.X. Wang, H. Zhou, T. Xu, X. Wang, X.L. Hu, H.W. Liu, X.P. Fan, W.H. Zheng, T.F. Yang, S.Z. Yang, Q.L. Zhang, X.L. Zhu, L.T. Sun, and A.L. Pan, Directional growth of ultralong $CsPbBr_3$ perovskite nanowires for high-performance photodetectors, *J. Am. Chem. Soc.*, 139(2017), No. 44, p. 15592.